Probing the dielectric response of the interfacial buffer layer in epitaxial graphene via optical spectroscopy

Heather M. Hill,[1] Albert F. Rigosi,[1,*] Sugata Chowdhury,[1] Yanfei Yang,[1,2] Nhan V. Nguyen,[1] Francesca Tavazza,[1] Randolph E. Elmquist,[1] David B. Newell,[1] and Angela R. Hight Walker[1]

[1]*Physical Measurement Laboratory, National Institute of Standards and Technology (NIST), Gaithersburg, Maryland 20899, USA*

[2]*Joint Quantum Institute, University of Maryland, College Park, Maryland 20742, USA*

(Received 12 September 2017; published 28 November 2017)

Monolayer epitaxial graphene (EG) is a suitable candidate for a variety of electronic applications. One advantage of EG growth on the Si face of SiC is that it develops as a single crystal, as does the layer below, referred to as the interfacial buffer layer (IBL), whose properties include an electronic band gap. Although much research has been conducted to learn about the electrical properties of the IBL, not nearly as much work has been reported on the optical properties of the IBL. In this work, we combine measurements from Mueller matrix ellipsometry, differential reflectance contrast, atomic force microscopy, and Raman spectroscopy, as well as calculations from Kramers-Kronig analyses and density-functional theory, to determine the dielectric function of the IBL within the energy range of 1 eV to 8.5 eV.

DOI: 10.1103/PhysRevB.96.195437

I. INTRODUCTION

Graphene has been widely demonstrated to have desirable electrical properties [1–3]. Additionally, epitaxial graphene (EG) growth on 4H-SiC substrate shows promise as a method to obtain homogeneous and single-crystal material, which can be fabricated into millimeter-sized devices, proving useful, especially in the field of metrology [4–10]. Even with all of its novel and exciting properties, graphene, whether obtained by exfoliation, chemical vapor deposition, or epitaxially from SiC, is inherently limited in its applications to the semiconductor industry due to its lack of a band gap.

Recently, there has been interest in garnering a more complete understanding of the interfacial buffer layer (IBL) that forms as a graphenelike, two-dimensional honeycomb atop and partially bound to the SiC substrate, specifically on the silicon face [11–14]. This IBL, being a by-product of the EG growth, exhibits a small band gap, a particularly sought-after property. Its electrical properties have been well-characterized by methods including scanning tunneling microscopy, low-energy electron diffraction, and angle-resolved photoemission spectroscopy [15–24]. A variety of theoretical studies have also been performed on the electronic structure of the IBL in 6H-, 4H-, and 3C-SiC substrates [25–30]. While the electronic properties are relatively known, there are significantly fewer works reported on the optical properties of the IBL, and one of those works characterizes the Raman signature of the IBL [31–33].

In this work, we report a full experimental and theoretical characterization of the IBL's dielectric function within the energy range of 1 eV to 8.5 eV, in the form $\varepsilon = \varepsilon_1 - i\varepsilon_2$, as obtained from Mueller matrix ellipsometry (MME), differential reflectance contrast (DRC), atomic force microscopy, Raman spectroscopy, Kramers-Kronig analysis, and density-functional theory (DFT).

*Corresponding author: albert.rigosi@nist.gov

II. EXPERIMENTAL METHODS

A. Sample preparation

Five IBL samples were prepared by first performing a full EG growth on square SiC chips diced from 100-mm 4H-SiC(0001) semi-insulating wafers (CREE) whose miscut angle was measured to be approximately 0.10°. SiC chips were rinsed with diluted hydrofluoric acid (<10%) followed by a deionized water bath. The chips were then oriented with the silicon face resting on a polished pyrolytic graphite substrate (SPI Glas 22). The observation of Newton's rings indicated that the chips were in close contact with the substrate, providing a diffusion barrier for escaping Si vapor to promote homogeneous growth conditions. The annealing process was performed in ambient argon with a graphite-lined resistive-element furnace (Materials Research Furnaces Inc.) [4]. Heating and cooling rates were approximately 1.5 °C/s and the process involved: (1) substrate cleaning at 1080 °C in a forming gas environment (96% Ar, 4% H_2 by volume) at 100 kPa for 30 min for surface hydrogenation [34,35]; (2) chamber evacuation and flush with 100 kPa Ar from a 99.999% liquid Ar source; and (3) a final growth stage performed at 1900 °C.

After the full EG growth, a 50-nm protective layer of Au was deposited onto the EG, followed by a protective polymer such as polymethyl methacrylate. The metallic layer helps prevent contamination from polymer residue. The thick layer of graphitic carbon that was formed on the C face of the samples was removed by reactive ion etching (RIE) with argon gas for 2 min (more details are available in Supplemental Material [36]). This removal restored the transparency of the substrate, which is crucial for differential reflectance contrast. After the carbon etch, a rectangular area of about 8 mm^2 on the C-face surface was roughened by a diamond-tipped etching tool to enable more accurate MME measurements by reducing backside reflections from the SiC for energies below its band gap. The full layer of EG, along with any small strips of bilayer epitaxial graphene which may form on the terrace edges, was then peeled away with a deposited layer of nickel [37,38], leaving the fully formed, single-crystal IBL exposed and ready for measurements.

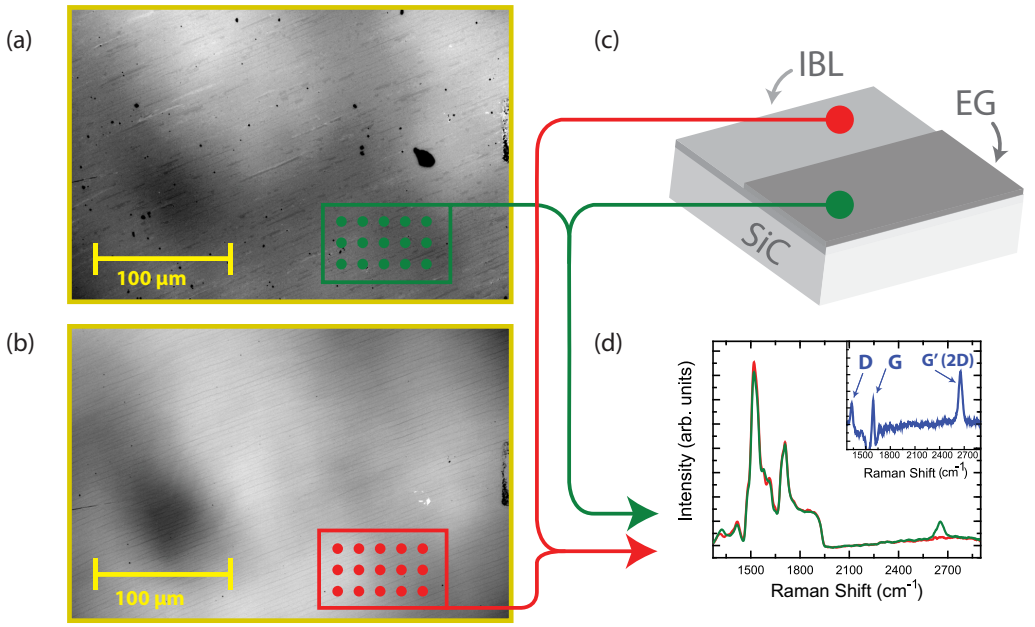

FIG. 1. (a) Optical image of a sample with complete graphene coverage was collected at 20× magnification. (b) The same region is optically imaged after the removal of the EG by peeling off deposited nickel. (c) An illustration is shown indicating where Raman spectra were collected. (d) Raman spectra were measured on the region with EG (shown as a green curve) and the region without EG (shown as a red curve) to verify that EG has been removed. The inset shows the resulting spectrum when the red curve is subtracted from the green curve, which should be the expected Raman curve from isolated EG.

Samples also had a portion of their surfaces etched away with RIE because the IBL cannot be peeled with nickel due to its strong bond to the SiC. Instead, portions of the IBL were exposed to 10 s of RIE, which was sufficient time to destroy most of the IBL, if we assume the carbon layer etches at a similar rate as graphene [39]. This allowed Raman, DRC, and MME measurement access to the SiC beneath the IBL as well as enabled the extraction of the optical constants for the SiC of each specific sample.

B. Differential reflectance contrast measurements

One of the two main optical techniques which was used for data collection was DRC. In DRC measurements, the samples were probed by a combined broadband emission from a halogen and deuterium lamp with a spot size of approximately 10 μm. The optical response of the IBL was characterized from the DRC spectra, which is labeled as $\Delta R/R$. Here, $\Delta R/R = (R_{\mathrm{IBL}} - R_{\mathrm{SiC}})/R_{\mathrm{SiC}}$, where R_{IBL} is the reflectance of the IBL on the substrate, and R_{SiC} denotes the reflectance of the bare SiC substrate. The reflected light was collected by a Filmetrics F20 spectrometer. All measurements were performed in air at room temperature over an energy range of 1.13 eV to 6.22 eV with 4-meV resolution.

C. Mueller matrix ellipsometry measurements

MME measurements were performed in a chamber filled with nitrogen gas at room temperature in a Woollam-302 vacuum-ultraviolet spectroscopic ellipsometer consisting of xenon and deuterium lamps covering the wavelength from about 145 to 1240 nm, with an elliptical spot size measuring approximately 2 × 4 mm. The photon energy ranged from 1 eV to 8.5 eV with 0.02-eV steps. MME measures the change in phase and polarization state of the light reflected from the sample, and the recorded data are converted by the software from Fresnel reflection coefficients representative of p- and s-polarized light (R_p and R_s) to the related quantities psi and delta (Ψ and Δ), where $\frac{R_p}{R_s} = e^{i\Delta}\tan\Psi$. Psi and delta can be further converted into optical constants of the probed material when a sufficient optical model is developed. Data were acquired at multiple angles of incidence, and because they are collected with Mueller matrix formalism, any effects from depolarization and minor sample inhomogeneity are accounted for and recorded in the data (an example of a full MME measurement is in Supplemental Material [36]). The main added advantages of MME over DRC are threefold: (1) The absence of water vapor and other potential unaccounted gases, which typically have a much higher absorption outside the visible range, do not interrupt the lamp light as it propagates to and from the sample, (2) increased measurement accuracy, and (3) a specialized modeling program, all of which allow for careful and rigorous treatment of the IBL. Despite the listed advantages of MME, DRC can still provide a reasonable estimate for the dielectric function of the IBL, one which reduces the traditionally large parameter space introduced by the WVASE32 modeling program for MME measured on unknown, thin materials.

D. Raman spectroscopy

Raman spectroscopy was also used to confirm the presence of the EG layer (before it was peeled), the IBL (postpeel), and the SiC directly beneath the IBL (post-RIE). Raman measurements were performed with a Renishaw InVia micro-Raman spectrometer using a 633-nm-wavelength excitation laser source. The spectra were measured and collected using a backscattering configuration, 1-μm spot size, 300-s acquisition time, 1.7-mW power, 50× objective, and 1200-mm^{-1}

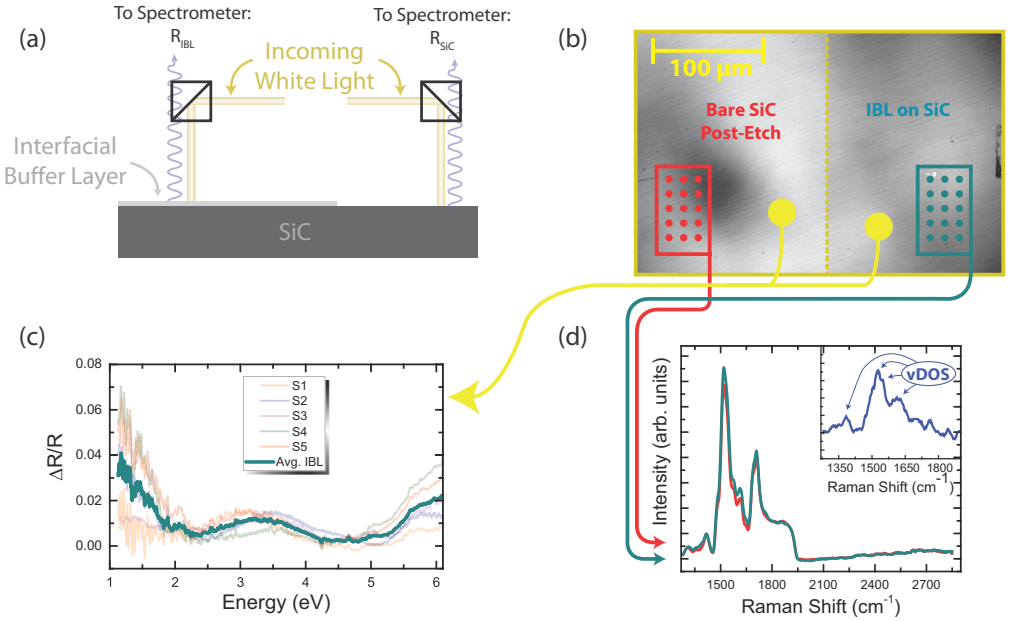

FIG. 2. (a) Schematic of the differential reflectance contrast measurement is shown. Generally, broadband light is directed to the IBL for one measurement and then the bare substrate in the next measurement. (b) Optical images of the same sample after and before etching away a submillimeter area of the IBL. (c) DRC measurements of the IBL. The five samples' spectra are shown in the transparent lines, and the average curve is shown in the opaque dark cyan. (d) Raman spectra averaged from maps indicated on the optical image in Fig. 1(b) taken on bare SiC (red curve) and the IBL on SiC (dark cyan). The inset shows the difference between the Raman spectrum with and without IBL to isolate the contribution from the IBL. The IBL response exhibits the same modes reported in Ref. [32].

grating. The Raman data clearly show that the EG was successfully removed as shown in Fig. 1. Rectangular Raman maps were also collected with step sizes of 20 μm in a 5×3 raster-style grid, as shown in Figs. 1(a) and 1(b) [with a measurement illustration shown in Fig. 1(c)]. The spectra were averaged for Fig. 1(d) and the IBL Raman was subtracted from the EG spectrum in the inset, yielding the expected response from isolated graphene. In the cases of Figs. 1(a) and 1(b), rapid optical characterization by use of a Nikon MM 400, as described in the literature [40,41], was used to identify homogeneous EG and lack thereof over the same rectangular area of about 8 mm^2 whose backside was scratched away. Raman spectra were collected for bare SiC regions that were formerly covered by the IBL, and subtracting the spectra yielded the expected Raman contribution of the IBL to the overall spectrum [see Fig. 2(d), which will be explored further] [32].

III. RAMAN AND DIFFERENTIAL RELECTANCE CONTRAST RESULTS

Once the IBL was characterized by Raman spectroscopy, DRC and MME measurements were performed. Before data for MME could be analyzed accurately and confidently, DRC data corresponding to the IBL optical response were needed.

The Raman measurements made on the IBL-on-SiC as well as the SiC-only region [depicted in Fig. 2(a)] are shown in Fig. 2(d), along with the difference of those two curves in the inset showing a response similar to what has been reported as a vibrational density of states for the IBL [32]. The five samples' measured DRC data are presented in Fig. 2(c) while a schematic of the DRC setup is shown in Fig. 2(a). The DRC data were averaged and used for subsequent analysis of the MME data. The MME schematic and an example of the IBL ellipsometric data Ψ and Δ are shown in Figs. 3(a) and 3(b), respectively. In Fig. 3(b), it becomes clear that the presence of the IBL lowers the measured values of Ψ for all three incident angles while the Δ takes on higher values. This change will be analyzed and modeled in more detail.

IV. ANALYZING MME DATA

A. Kramers-Kronig analysis on DRC data

Kramers-Kronig analysis was used to extract the dielectric function from the DRC measurements, as has been implemented in the analysis of other two-dimensional materials and their DRC spectra [43,44]. In the limit of a thin material on a transparent substrate, an approximation, given in Eq. (1), can be used to relate the DRC to the absorption (A) of the material. In previous works on graphene and other two-dimensional materials, the optical constants of the transparent substrate are approximated as purely real and constant [45]. In the case of SiC, it is invalid to treat the optical constants as purely real and constant. Therefore, the optical constants (and by extension, the dielectric function) of SiC, here denoted by n_{SiC} and k_{SiC}, which incorporate both real and imaginary response behavior, must be obtained before we can use this equation.

$$\frac{\Delta R}{R} = \frac{4}{n_{\mathrm{SiC}}^2 + k_{\mathrm{SiC}}^2 - 1} A \tag{1}$$

The dielectric function of SiC was calculated directly from the corresponding MME measurement for each of the five samples. Using this dielectric function, an approximate absorption of the IBL can be calculated from the DRC using

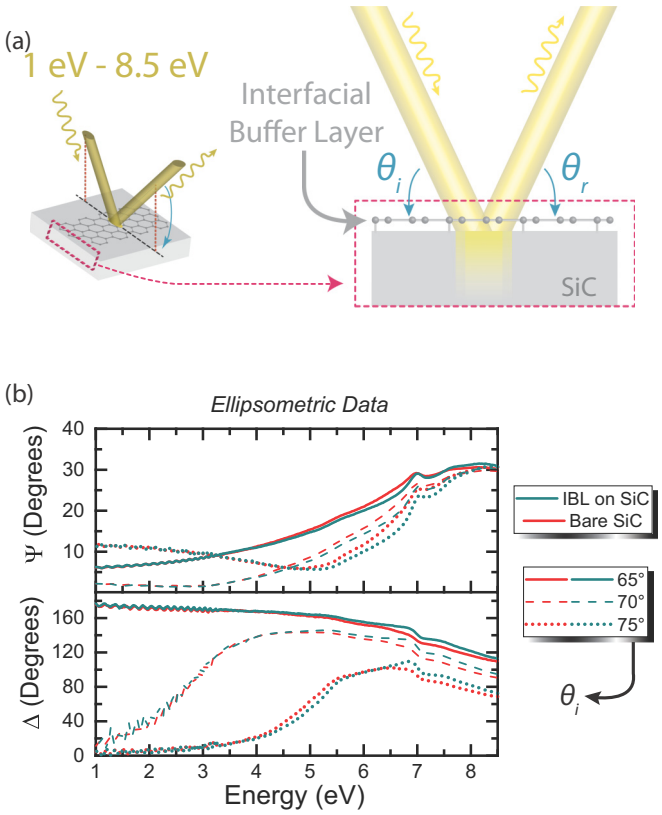

FIG. 3. (a) Schematic of the Mueller matrix ellipsometer measurement is shown. Broadband light is directed to the IBL at variable incident angles, and the tool evaluates the change in polarization and intensity as a function of the incident angle. (b) Representative set of raw data from one of the IBL samples, showing the Ψ in the top half and Δ in the bottom half, both measured at three different angles of incidence. The feature pronounced around 7 eV has been reported as a critical point energy of optical transitions in the out-of-plane dielectric function of 4H-SiC [42].

Eq. (1). The approximated absorption gives an *initial estimate* of the shape of the imaginary part of the dielectric function (ε_2), which then undergoes an iterative process that optimizes the accuracy of the dielectric function extracted from DRC measurements. The absorption range was artificially set to zero outside the measured energy range since the Kramers-Kronig relations assume that the optical behavior of the sample for all energies is known. We multiplied our absorption spectrum by the factor $\frac{\varepsilon_2}{A(E)} = \frac{\hbar c}{EL}$, where E is the energy and L is the layer thickness. This factor is a ratio of ε_2-to-absorption seen in other two-dimensional materials [43,44,46]. We then used the Kramers-Kronig relation shown below:

$$\varepsilon_1(E) = 1 + \frac{1}{\pi}\int_{-\infty}^{\infty} \frac{\varepsilon_2(E')}{E' - E} dE' \qquad (2)$$

Using our initial ε_2 and Eq. (2), we obtain a full dielectric function (labeled $\varepsilon_1^{GEN} - i\varepsilon_2^{GEN}$ to indicate that it was generated). To check that our generated dielectric is reasonable, we compute a DRC spectrum using our generated dielectric function and standard thin-film analysis to compare to the raw data [47]. Many differences are observed between the first generated DRC curve and the original DRC data. We use an iterative fitting procedure to generate a DRC curve that best fits the measured DRC curve. To do so we: (1) Subtract the generated DRC curve and the original DRC data to yield a "DRC error curve". (2) Convert the DRC error curve into an absorption error curve using Eq. (1) and multiply by the factor $\frac{\hbar c}{EL}$ to get an "ε_2 error curve". (3) Add the ε_2 error curve onto the previous ε_2^{GEN} function to make an incrementally more accurate ε_2^{GEN+1}. (4) Calculate a new ε_1^{GEN+1} via Eq. (2). (5) Use $\varepsilon_1^{GEN+1} - i\varepsilon_2^{GEN+1}$ to generate another DRC curve. (6) Compare this new curve to the original data, and repeat the iteration (steps 1 to 6) until the standard deviation of the difference of the curves is below 10^{-4}.

B. Extracting the dielectric function from MME data

Using Kramers-Kronig analysis, the dielectric function of the IBL was extracted within the energy range of 1.13 eV to 6.22 eV, with 4-meV resolution, as shown in Fig. 4(a). The DRC calculated from the final generated dielectric function is also shown in Fig. 4(a) to demonstrate the excellent agreement between the calculated and experimental data. The final generated dielectric function was smoothed with ten-point adjacent averaging and converted into a file format compatible with the WVASE32 modeling program. For each sample, both the IBL and the SiC (from the same region, post-RIE) were measured, and therefore each sample had a slightly different SiC layer model. After confirming the 0.5-mm-thick SiC model, another model was built to calculate the dielectric function of the IBL for the range 1 eV to 8.5 eV. The model consisted of three layers, starting from the bottom up: (1) a 0.5-mm-thick SiC layer with optical constants based on the measured values of that sample, (2) an IBL of thickness 0.25 nm, as documented in the literature (Refs. [13,16]), and (3) a layer that is represented by a Bruggeman effective medium approximation (EMA) [48]. The EMA layer, which traditionally simulates effects of surface roughness, was developed with 16% IBL, 42% SiC, and 42% void (where no material is present). More details on the use of the EMA are provided in Supplemental Material [36].

The remaining free parameters were the optical constants (dielectric function) of the IBL and the thickness of the EMA. Multiple models were calculated with varying EMA thickness until the chi-squared error between the average measured DRC and MME IBL dielectric function in the range of 2 eV to 5 eV was minimized. This energy range was selected due to larger instrument errors at the endpoints of the spectrum. With an EMA thickness of 1.5 nm, the real and imaginary parts of the optimal dielectric function were extracted, smoothed with five-point adjacent averaging, and plotted, along with its uncertainty, in Fig. 4(b). The less-accurate dielectric function generated by Kramers-Kronig analysis on the experimental DRC is also included in Fig. 4(b), shown as the dotted curves. The vertical axis of the real part is half of the range of the imaginary component, and the inset of the imaginary component has a vertical axis one-sixth of the total range. The shaded green indicates the uncertainty provided by the modeling program.

C. Comparison with density-functional theory calculations

Calculations were carried out using DFT as implemented in plane-wave self-consistent field (PWSCF) code [49–51], using

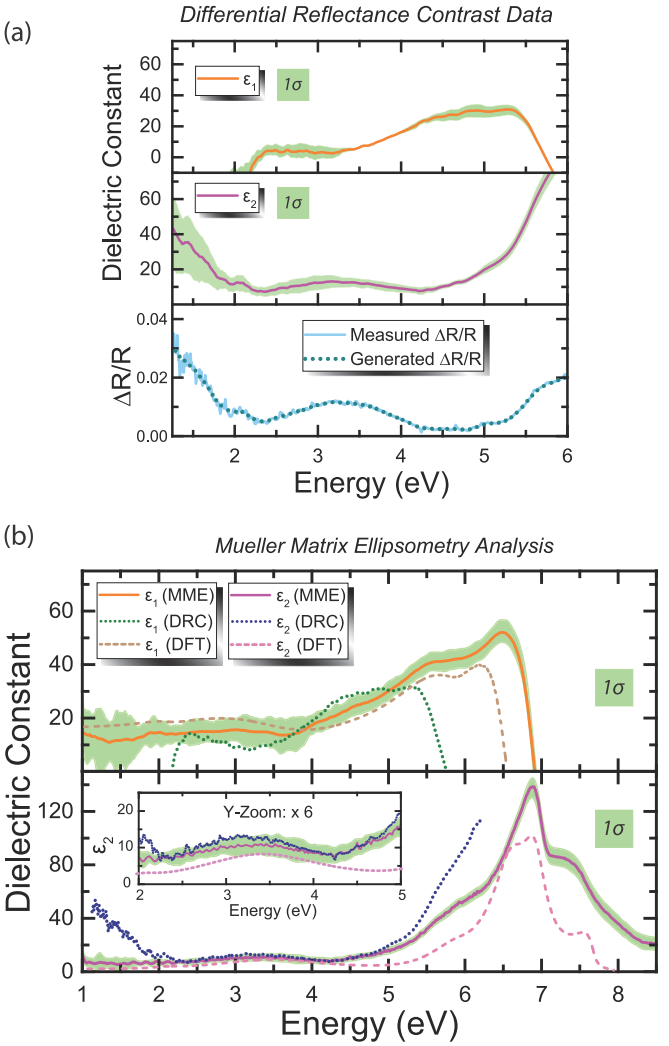

FIG. 4. (a) Average DRC data in the bottom third of the graph was decomposed into its respective dielectric function, with the real part occupying the top third and the imaginary part occupying the middle third. The shaded green indicates the propagated uncertainty of the average DRC curve. In the bottom third, the dotted dark cyan is a generated DRC curve based on the calculated dielectric function in the top two thirds and compared to the data. (b) The final extracted dielectric function for the IBL is shown here, with the real part in the top half and the imaginary part in the bottom half. The function is found via MME for the range 1 eV to 8.5 eV and is compared to those found with the DRC data and Kramers-Kronig analysis (dotted lines) and DFT calculations (dashed lines). The inset in the bottom half is a vertically zoomed area for clarity. For all curves, the shaded green indicates the uncertainty of the MME measurement.

the projector-augmented wave method within the generalized gradient approximation [52]. For the electronic structure calculations, an $8 \times 8 \times 8$ k-point grid and a $13 \times 13 \times 1$ k-point grid was used for the unit-cell and slab calculations, respectively. To investigate the general optical properties, a $5 \times 5 \times 1$ k-point grid was used. To calculate the dielectric function of the IBL [53,54], the Liouville-Lanczos approach was applied to linear-response time-dependent DFT and to PWSCF. The result is compared with the experimental data in Fig. 4(b), where DFT curves are represented as dashed lines. More information on the DFT calculations is provided in Supplemental Material [36]. The DFT calculations strongly support the MME data in terms of the positions of various features, notably in the imaginary portion of the dielectric function. The several features at 3.4 eV, 5.8 eV, and 6.84 eV and the pronounced shoulder above 7 eV are well-represented in the DFT calculations. Furthermore, the extracted band gap from these calculations yields approximately 0.3 eV, which is comparable to the result found in the recent IBL work [13].

V. CONCLUSIONS

In conclusion, we performed a full experimental and theoretical characterization of the IBL's dielectric function for the energy range 1 eV to 8.5 eV from Mueller matrix ellipsometry, differential reflectance contrast, Kramers-Kronig, and DFT analyses. The DRC measurements provide both an initial approximation of the dielectric function and a secondary comparison to the MME measurements. Using the initial dielectric function to fit the MME data, we extract a more accurate IBL dielectric function over a larger range of energies. The IBL is a high-mobility, narrow-band-gap semiconductor that has the advantage of chip-scale growth. This work is a rigorous investigation of dielectric function of the IBL, and a step toward understanding the optical properties and band structure of this promising 2D material.

ACKNOWLEDGMENTS

Work done by Y.Y. was supported by Federal Grant No. 70NANB12H185. A.F.R. and H.M.H. would like to thank the National Research Council's Research Associateship Program for the opportunity. We would like to thank Alex Boosalis and Thomas Germer for fruitful discussions.

H.M.H. and A.F.R. designed the experiment, collected and analyzed data. S.C. provided theoretical calculations. Y.Y. and R.E.E. produced graphene samples. The manuscript was written through contributions of all authors. All authors have given approval to the final version of the manuscript. The authors declare no competing financial interest. Commercial equipment, instruments, and materials are identified in this paper in order to specify the experimental procedure adequately. Such identification is not intended to imply recommendation or endorsement by the National Institute of Standards and Technology or the United States government, nor is it intended to imply that the materials or equipment identified are necessarily the best available for the purpose.

H.M.H. and A.F.R. contributed equally to this work.

[1] A. K. Geim and K. S. Novoselov, Nat. Mater. **6**, 183 (2007).

[2] K. S. Novoselov, A. K. Geim, S. V. Morozov, D. Jiang, Y. Zhang, S. V. Dubonos, I. V. Grigorieva, and A. A. Firsov, Science **306**, 666 (2004).

[3] K. S. Novoselov, V. I. Fal'ko, L. Colombo, P. R. Gellert, M. G. Schwab, and K. A. Kim, Nature (London) **490**, 192 (2012).

[4] Y. Yang, G. Cheng, P. Mende, I. G. Calizo, R. M. Feenstra, C. Chuang, C.-W. Liu, G. R. Jones, A. R. Hight Walker, and R. E. Elmquist, Carbon **115**, 229 (2017).

[5] A. F. Rigosi, N. R. Glavin, C.-I. Liu, Y. Yang, J. Obrzut, H. M. Hill, J. Hu, H.-Y. Lee, A. R. Hight Walker, C. A. Richter, R. E. Elmquist, and D. B. Newell, Small **13**, 1700452 (2017).

[6] A. F. Rigosi, C.-I. Liu, N. R. Glavin, Y. Yang, H. M. Hill, J. Hu, A. R. Hight Walker, C. A. Richter, R. E. Elmquist, and D. B. Newell, ACS Omega **2**, 2326 (2017).

[7] A. Tzalenchuk, S. Lara-Avila, A. Kalaboukhov, S. Paolillo, M. Syväjärvi, R. Yakimova, O. Kazakova, T. J. B. M. Janssen, V. Fal'ko, and S. Kubatkin, Nat. Nanotechnol. **5**, 186 (2010).

[8] R. Ribeiro-Palau, F. Lafont, J. Brun-Picard, D. Kazazis, A. Michon, F. Cheynis, O. Couturaud, C. Consejo, B. Jouault, W. Poirier, and F. Schopfer, Nat. Nanotechnol. **10**, 965 (2015).

[9] T. J. B. M. Janssen, A. Tzalenchuk, R. Yakimova, S. Kubatkin, S. Lara-Avila, S. Kopylov, and V.I. Fal'ko, Phys. Rev. B **83**, 233402 (2011).

[10] Y. Fukuyama, R. E. Elmquist, L.-I. Huang, Y. Yang, F.-H. Liu, and N.-H. Kaneko, IEEE Trans. Instrum. Meas. **64**, 1451 (2015).

[11] M. S. Nevius, M. Conrad, F. Wang, A. Celis, M. N. Nair, A. Taleb-Ibrahimi, A. Tejeda, and E. H. Conrad, Phys. Rev. Lett. **115**, 136802 (2015).

[12] I. Shtepliuk, T. Iakimov, V. Khranovskyy, J. Eriksson, F. Giannazzo, and R. Yakimova, Crystals **7**, 162 (2017).

[13] M. N. Nair, I. Palacio, A. Celis, A. Zobelli, A. Gloter, S. Kubsky, J.-P. Turmaud, M. Conrad, C. Berger, W. de Heer, E. H. Conrad, A. Taleb-Ibrahimi, and A. Tejada, Nano Lett. **17**, 2681 (2017).

[14] M. Conrad, F. Wang, M. S. Nevius, K. Jinkins, A. Celis, M. N. Nair, A. Tejeda, Y. Garreau, A. Vlad, A. Coati, P. F. Miceli, E. H. Conrad, and A. Taleb-Ibrahimi, Nano Lett. **17**, 341 (2017).

[15] G. M. Rutter, N. P. Guisinger, J. N. Crain, E. A. A. Jarvis, M. D. Stiles, T. Li, P. N. First, and J. A. Stroscio, Phys. Rev. B **76**, 235416 (2007).

[16] H. Huang, W. Chen, S. Chen, and A. T. S. Wee, ACS Nano **2**, 2513 (2008).

[17] P. Mallet, F. Varchon, C. Naud, L. Magaud, C. Berger, and J.-Y. Veuillen, Phys. Rev. B **76**, 041403 (2007).

[18] C. Riedl, U. Starke, J. Bernhardt, M. Franke, and K. Heinz, Phys. Rev. B **76**, 245406 (2007).

[19] W. Chen, H. Xu, L. Liu, X. Gao, D. Qi, G. Peng, S. C. Tan, Y. Feng, K. P. Loh, and A. T. S. Wee, Surf. Sci. **596**, 176 (2005).

[20] K. V. Emtsev, F. Speck, T. Seyller, L. Ley, and J. D. Riley, Phys. Rev. B **77**, 155303 (2008).

[21] I. Forbeaux, J. M. Themlin, and J. M. Debever, Phys. Rev. B **58**, 16396 (1998).

[22] T. Seyller, K. V. Emtsev, K. Gao, F. Speck, L. Ley, A. Tadich, L. Broekman, J. D. Riley, R. C. G. Leckey, O. Rader, A. Varykhalov, and A. M. Shikin, Surf. Sci. **600**, 3906 (2006).

[23] T. Ohta, A. Bostwick, J. L. McChesney, T. Seyller, K. Horn, and E. Rotenberg, Phys. Rev. Lett. **98**, 206802 (2007).

[24] S. Y. Zhou, G.-H. Gweon, J. Graf, A. V. Fedorov, C. D. Spataru, R. D. Diehl, Y. Kopelevich, D.-H. Lee, S. G. Louie, and A. Lanzara, Nat. Phys. **2**, 595 (2006).

[25] F. Varchon, R. Feng, J. Hass, X. Li, B. N. Nguyen, C. Naud, P. Mallet, J.-Y. Veuillen, C. Berger, E. H. Conrad, and L. Magaud, Phys. Rev. Lett. **99**, 126805 (2007).

[26] E. Lampin, C. Priester, C. Krzeminski, and L. Magaud, J. Appl. Phys. **107**, 103514 (2010).

[27] X. Peng and R. Ahuja, Nano Lett. **8**, 4464 (2008).

[28] M. Inoue, H. Kageshima, Y. Kangawa, and K. Kakimoto, Phys. Rev. B **86**, 085417 (2012).

[29] A. Mattausch and O. Pankratov, Phys. Status Solidi B **245**, 1425 (2008).

[30] S. Kim, J. Ihm, H. J. Choi, and Y.-W. Son, Phys. Rev. Lett. **100**, 176802 (2008).

[31] F. Nelson, A. Sandin, D. B. Dougherty, D. E. Aspnes, J. E. Rowe, and A. C. Diebold, J. Vac. Sci. Technol. B **30**, 04E106 (2012).

[32] F. Fromm, M. H. Oliveira, A. Molina-Sánchez, M. Hundhausen, J. M. J. Lopes, H. Riechert, L. Wirtz, and T. Seyller, New J. Phys. **15**, 043031 (2013).

[33] K. Megasari, E. Widianto, V. Efelina, K. Abraha, A.T.S. Wee, A. Rusydi, and I. Santoso, AIP Conf. Proc. **1755**, 150014 (2016).

[34] J. Schardt, C. Bram, S. Müller, U. Starke, K. Heinz, and K. Müller, Surf. Sci. **405**, 232 (1995).

[35] T. Seyller, J. Phys. Condens. Matter **16**, S1755 (2004).

[36] See Supplemental Material at http://link.aps.org/supplemental/10.1103/PhysRevB.96.195437 for EG growth, sample preparation, additional DRC and MME data, additional information about the IBL, optical modeling techniques, and more details on DFT calculations. This material includes Refs. [55–65].

[37] J. Kim, H. Park, J. B. Hannon, S.W. Bedell, K. Fogel, D. K. Sadana, and C. Dimitrakopoulos, Science **342**, 833 (2013).

[38] S.-H. Bae, X. Zhou, S. Kim, Y. S. Lee, S. S. Cruz, Y. Kim, J. B. Hannon, Y. Yang, D. K. Sadana, F. M. Ross, H. Park, and J. Kim, Proc. Natl. Acad. Sci. USA **114**, 4082 (2017).

[39] I. Childres, L. A. Jauregui, J. Tian, and Y. P. Chen, New J. Phys. **13**, 025008 (2011).

[40] V. Panchal, Y. Yang, G. Cheng, J. Hu, C.-I. Liu, A. F. Rigosi, C. Melios, O. Kazakova, A. R. Hight Walker, D. B. Newell, and R. E. Elmquist, arXiv:1711.03563 [Nat. Commun. (to be published)].

[41] T. Yager, A. Lartsev, S. Mahashabde, S. Charpentier, D. Davidovikj, A. Danilov, R. Yakimova, V. Panchal, O. Kazakova, A. Tzalenchuk, S. Lara-Avila, and S. Kobatkin, Nano Lett. **13**, 4217 (2013).

[42] O. P. A. Lindquist and K. Jarrendahl, Appl. Phys. Lett. **78**, 2715 (2001).

[43] A. F. Rigosi, H. M. Hill, Y. L. Li, A. Chernikov, and T. F. Heinz, Nano Lett. **15**, 5033 (2015).

[44] Y. Li, A. Chernikov, X. Zhang, A. Rigosi, H. M. Hill, A. M. van der Zande, D. A. Chenet, E.-M. Shih, J. Hone, and T. F. Heinz, Phys. Rev. B **90**, 205422 (2014).

[45] K. F. Mak, M. Y. Sfeir, Y. Wu, C. H. Lui, J. A. Misewich, and T. F. Heinz, Phys. Rev. Lett. **101**, 196405 (2008).

[46] D. Kecik, C. Bacaksiz, R. T. Senger, and E. Durgun, Phys. Rev. B **92**, 165408 (2015).

[47] E. Hecht, *Optics,* 4th ed. (Addison-Wesley, San Francisco, 2002), p. 426.

[48] D. A. G. Bruggeman, Ann. Phys. **5**, 636 (1935).

[49] P. Hohenberg and W. Kohn, Phys. Rev. **136**, B864 (1964).

[50] W. Kohn and L. J. Sham, Phys. Rev. **140**, A1133 (1965).

[51] P. Giannozzi, S. Baroni, N. Bonini, M. Calandra, R. Car, C. Cavazzoni, D. Ceresoli, G. L. Chiarotti, M. Cococcioni, I. Dabo, A. Dal Corso, S. de Gironcoli, S. Fabris, G. Fratesi, R. Gebauer, U. Gerstmann, C. Gougoussis, A. Kokalj, M. Lazzeri,

L. Martin-Samos, N. Marzari, F. Mauri, R. Mazzarello, S. Paolini, A. Pasquarello, L. Paulatto, C. Sbraccia, S. Scandolo, G. Sclauzero, A. P. Seitsonen, A. Smogunov, P. Umari, and R. M. Wentzcovitch, J. Phys.: Condens. Matter **21**, 395502 (2009).

[52] J. P. Perdew, K. Burke, and M. Ernzerhof, Phys. Rev. Lett. **77**, 3865 (1996).

[53] I. Timrov, N. Vast, R. Gebauer, and S. Baroni, Phys. Rev. B **88**, 064301 (2013).

[54] I. Timrov, N. Vast, R. Gebauer, and S. Baroni, Comput. Phys. Commun. **196**, 460 (2015).

[55] A. Boosalis, T. Hofmann, V. Darakchieva, R. Yakimova, and M. Schubert, Appl. Phys. Lett. **101**, 011912 (2012).

[56] F. J. Nelson, V. K. Kamineni, T. Zhang, E. S. Comfort, J. U. Lee, and A. C. Diebold, App. Phys. Lett. **97**, 253110 (2010).

[57] D.-H. Chae, T. Utikal, S. Weisenburger, H. Giessen, K. von Klitzing, M. Lippitz, and J. Smet, Nano Lett. **11**, 1379 (2011).

[58] K. F. Mak, J. Shan, and T. F. Heinz, Phys. Rev. Lett. **106**, 046401 (2011).

[59] B. Singh, A. Diwan, V. Jain, A. Herrera-Gomez, J. Terry, and M. R. Linford, Appl. Surf. Sci. **387**, 155 (2016).

[60] V. R. Cooper, Phys. Rev. B **81**, 161104 (2010).

[61] D. Vanderbilt, Phys. Rev. B **41**, 7892 (1990).

[62] M. E. Levinshtein, S. L. Rumyantsev, and M. S. Shur, *Properties of Advanced Semiconductor Materials: GaN, AIN, InN, BN, SiC, SiGe* (John Wiley & Sons, Hoboken, NJ, 2001).

[63] H. Schulz and K. Thiemann, Solid State Commun. **32**, 783 (1979).

[64] M. C. Payne, M. P. Teter, D. C. Allan, T. Arias, and J. Joannopoulos, Rev. Mod. Phys. **64**, 1045 (1992).

[65] M. Stockmeier, R. Müller, S. Sakwe, P. Wellmann, and A. Magerl, J. Appl. Phys. **105**, 033511 (2009).